University of Massachusetts Amherst

2013

Filamentary Accretion Flows in the Embedded Serpens South Protocluster

Helen Kirk
Philip C. Myers
Tyler L. Bourke
R. A Gutermuth, *University of Massachusetts - Amherst*
Abigail Hedden, et al.

FILAMENTARY ACCRETION FLOWS IN THE EMBEDDED SERPENS SOUTH PROTOCLUSTER

Helen Kirk[1,2], Philip C. Myers[1], Tyler L. Bourke[1], Robert A. Gutermuth[3], Abigail Hedden[4], Grant W. Wilson[3]

ABSTRACT

One puzzle in understanding how stars form in clusters is the source of mass – is all of the mass in place before the first stars are born, or is there an extended period when the cluster accretes material which can continuously fuel the star formation process? We use a multi-line spectral survey of the southern filament associated with the Serpens South embedded cluster-forming region in order to determine if mass is accreting from the filament onto the cluster, and whether the accretion rate is significant. Our analysis suggests that material is flowing along the filament's long axis at a rate of $\sim$ 30 $M_\odot$ Myr^{-1} (inferred from the N_2H^+ velocity gradient along the filament), and radially contracting onto the filament at $\sim$ 130 $M_\odot$ Myr^{-1} (inferred from HNC self-absorption). These accretion rates are sufficient to supply mass to the central cluster at a similar rate to the current star formation rate in the cluster. Filamentary accretion flows may therefore be very important in the ongoing evolution of this cluster.

1. INTRODUCTION

Understanding how clusters of stars form is a topic of considerable interest, since most stars appear to form within clustered environments (e.g., Lada & Lada 2003; Bressert et al 2010). As noted in Myers (2011a), young stellar clusters are tightly packed with stars in their centres; the initial gas mass density inferred to create these stars is significantly higher than observed formation conditions. One simple solution to this problem is to feed in additional mass as the cluster is forming. Analysis of competitive accretion simulations indeed show that this can occur (Smith et al 2009). Observationally, young embedded cluster-forming systems are often found to be associated with multiple filaments, in a hub-spoke like geometry (e.g., Myers 2009a). Recent *Herschel* observations have shown that filaments are ubiquitous in star-forming regions, and furthermore that prestellar cores and protostars tends to be associated only with those filaments which are gravitationally supercritical (André et al 2010). Filaments therefore appear to be the prime candidate for providing a continuous source of material to be accreted onto forming clusters. Few observations yet exist, however, to test this idea, as most have focussed on the column density structure of filaments and clusters (e.g., Arzoumanian et al 2011).

Several decades ago, low resolution CO observations showed that some filaments have velocity gradients running along their length (on $\sim$ 10 pc scales, e.g., McCutcheon et al 1982; Dobashi et al 1992). Additionally, some filaments had hints of a velocity gradient across their short axis (e.g., Uchida et al 1990; Dobashi et al 1992). Higher resolution observations of dense gas species, however, have been lacking until recently. Hacar & Tafalla (2011) observed the low-mass

star-forming region L1517 in Taurus, and showed it contains several coherent, roughly thermal filaments which are well-fit by an isothermal cylinder model. These filaments have small modulations in their (column) density and velocity profiles along the long axis, suggesting core accretion from the surrounding filament material. Hacar et al (in prep) conducted a similar study of the filaments in B213 in Taurus, finding evidence that the singular filament visible in column density maps is actually composed of many distinct velocity components of gas, each of which has a coherent and thermal velocity profile. In more massive filaments, spectral observations tend to indicate much more dynamic gas motions. Miettinen (2012) made pointed observations of $C^{18}O$ and $C^{17}O$ dense clumps embedded in the filamentary IRDC G304.74+01.32 and find strong signs of infall and strongly non-thermal linewidths. If the non-thermal linewidths can be interpreted as providing additional support, then the clumps and filament may be in virial equilibrium. In the DR21 filament, Schneider et al (2010) find signatures of infalling motion over both the filament and clump scales, and kinematic signatures consistent with the filament forming from converging flows.

In order to study the question of filament accretion onto clusters, we present kinematic observations of the Serpens South embedded cluster and surrounding filaments. To the best of our knowledge, this is the first study to obtain sufficient complementary measurements of the gas velocity to provide reasonable certainty in attributing the motions to filamentary accretion.

The Serpens South cluster was first discovered in 2008 by Gutermuth et al from *Spitzer* data. In this discovery paper, the cluster is clearly embedded in a dense filamentary structure which shows up in absorption at 8 μm. Gutermuth et al (2008) identify approximately 90 YSOs, and find that the ratio of class II to I sources in the region is low, around 0.7, which is much lower than the median value of 3.7 in nearby cluster-forming regions (Gutermuth et al 2009), and suggests that the Serpens South embedded cluster is among the youngest examples known. As such, Serpens South may be a particu-

[1] Radio and Geoastronomy Division, Harvard Smithsonian Center for Astrophysics, MS-42, Cambridge, MA, 02138, USA
[2] Currently a Banting Fellow at the Origins Institute, McMaster University; kirkh@mcmaster.ca
[3] Department of Astronomy, University of Massachusetts Amherst
[4] Army Research Labs, Maryland

larly good target to search for accretion flows in filaments and onto the central cluster, since there will have been less time for stellar feedback to disrupt or complicate the cluster-forming gas motions. Based on their *Spitzer* data, Gutermuth et al (2008) estimate that stars are forming in the central cluster at a rate of 90 $M_\odot$ Myr^{-1}, although more recent work by Maury et al (2011) using a combination of *Spitzer*, *Herschel*, and MAMBO 1.2 mm dust continuum observations suggest that the rate may be several times smaller. Much of this discrepancy is due to the timescales assumed for protostellar evolution.

Additional recent observations of Serpens South include near-IR polarization measurements suggesting a relatively uniform magnetic field aligned perpendicular to the main filamentary structure (Sugitani et al 2011), and a catalog of protostars associated with outflows suggesting that the energy injected in the central embedded cluster by the outflows may be enough to maintain the current level of non-thermal motion (Nakamura et al 2011). X-ray observations from *Chandra* combined with the *Spitzer* data show that the YSOs have similar properties to those in Serpens Main and NGC 1333 (e.g., Winston et al 2010), with analysis suggesting that the class III sources are likely a by-product of early disk-stripping from inter-cluster dynamics, rather than indicating a population older than the class II sources (Winston et al, in prep).

We obtained spectral line maps with Mopra[5] across $\sim$100 $arcmin^2$ of the main filament in Serpens South in a variety of molecular tracers (discussed in the next section) in order to measure the motion of the dense gas in the filaments. We combine this data with measurements of the column density distribution (Gutermuth et al, in prep) obtained with ASTE using the AzTEC camera (Wilson et al 2008) to fully interpret the dynamical state of the filaments. Using these data, we find strong evidence that filamentary accretion flows are playing an important role in the ongoing evolution of the Serpens South cluster.

In Section 2, we discuss our Mopra observations, and the basic filamentary structure seen in Section 3. In Sections 4 and 5, we discuss analyze the spectral data and estimate the filamentary accretion rates. In Section 6, we perform some simple analysis of the column density structure of the filament, then discuss our main results in Section 7, and conclude in Section 8.

2. OBSERVATIONS

2.1. *Data*

Our observations were made with the ATNF Mopra 22 m telescope in Australia, in September 2008, using the single pixel broadband spectrometer, MOPS[6]. MOPS allows for multiple spectral windows to be observed simultaneously, increasing the mapping efficiency for multiple spectral lines; the spectral resolution in the zoom mode is $\sim$0.108 km s^{-1} for the 90 GHz receiver. We used eight zoom windows to focus on different molecules of interest

– the (1–0) transitions of N_2H^+, HNC, HCN, $H^{13}CN$, HCO^+, $H^{13}CO^+$, plus SiO(2–1) and $NH_2D(1,1)$. Most of these transitions trace dense gas; HCO^+ is sensitive to outflows, while SiO traces primarily shocked emission (see, e.g., Sanhueza et al 2012; Bergin & Tafalla 2007; Vasyunina et al 2011, for a discussion on the physical conditions traced by these molecules).

We made on-the-fly maps, scanning along R.A., and Dec., with $11''$ spacing between scan rows, and a scan speed of $3.71''$ s^{-1}. Square maps of $5.3'$ per side (with the inner $5'$ fully sampled) were made and later placed on a single grid using Gridzilla. An OFF position of ($18^h16^m56^s$, $+03^o02'19''$) was observed roughly every three minutes, and a measurement of the system temperature taken every thirteen minutes. Every map required roughly an hour of integration time for each of the R.A. and Dec. scans. We used Livedata[3] to apply the bandpass calibration and remove a low order polynomial baseline. We then created uniformly gridded spectral cubes for each waveband using Gridzilla[7], using a final pixel size of $15''$; Mopra's spatial resolution is $\sim40''$ at 3 mm (Ladd et al 2005). We converted the spectra from T_a^* to T_{mb} units using an antenna efficiency of 0.49 (Ladd et al 2005). Due to the relatively large separation between the adopted OFF position and our mapping area, with this initial reduction, we found some spectra still showed significant ripples in their baseline. In these cases, CLASS[8] was used to fit and remove a higher order polynomial baseline.

Figure 1 shows the region we mapped with Mopra, compared to a dust emission map recently obtained with AzTEC/ASTE by Gutermuth et al (in prep). In Figure 1, the greyscale image and contours show the dust emission, while the blue contour shows the area we mapped with Mopra. The yellow diamonds, orange open circles, and red filled circles show the YSOs identified by Gutermuth in a re-analysis of the data in Gutermuth et al (2008) which now includes *Spitzer* 24 μm data, and adopts the classification scheme of Gutermuth et al (2009). Clearly, the Mopra observations span the main filamentary structure in Serpens South. In total, we have more than 1500 spectra at each of the 8 wavebands, and cover an area of roughly 100 $arcmin^2$. The median value of the rms noise per channel in the spectra are $\sim$0.34 K km s^{-1} for all eight molecular species. Table 1 summarizes the central frequency adopted for each line and the associated reference. For lines with hyperfine structure, the transition associated with the adopted frequency is also listed.

2.2. *Line Fitting*

For the emission lines without hyperfine structure (HCO^+, $H^{13}CO^+$, and SiO)[9], we fit each spectrum with a single Gaussian, using the least squares minimization code MPFIT (Markwardt 2008, see also http://purl.com/net/mpfit) to constrain the fit pa-

---

rameters to a reasonable range and calculate the errors associated with each fitting parameter. We similarly fit NH_2D with a single Gaussian, as the line was sufficiently weak that none of the hyperfine satellites were detected (in most cases, not even the central component was visible). For these four transitions, the parameters fit are the velocity centroid, velocity dispersion (in Gaussian sigma units), and line peak.

For the emission lines with hyperfine structure (N_2H^+, HNC, HCN, and $H^{13}CN$), we substitute the Gaussian model with a single uniform slab model with the appropriate hyperfine emission information (adapted from Rosolowsky et al 2008), and again use MPFIT to find the best fitting line parameters – in this case, the velocity centroid, velocity dispersion (in Gaussian sigma units), optical depth, and excitation temperature.

For all of the results discussed in this paper, we only analyze spectra which are above a signal to noise level of 3.5 – i.e., we require an integrated intensity to be 3.5 times that expected from the noise level (the spectral rms times the square root of the number of velocity channels), and also a minimum of two spectral channels showing emission about 3.5 times the spectral rms (using two channels instead of one decreases the likelihood of the emission being a noise spike). Calculation of the integrated intensity is discussed in Section 3.

Over nearly the entire area mapped, most of the emission lines detected show strong indications of self-absorption; only N_2H^+, $H^{13}CO^+$, and, where detected, NH_2D appears single-peaked, while SiO has no unambiguous detections. Even the N_2H^+ lines may be mildly self-absorbed in some locations, but our signal to noise and spectral resolution are insufficient to determine this definitively. Figure 2 shows the spectrum of all eight emission lines near the cluster centre, at the location where the N_2H^+ emission is strongest, ($-18^h30^m01^s, -2^o03'12"$). In all cases, the spectra have been summed over the nearest four by four pixels ($60''$) to increase the signal to noise. The red vertical lines indicate the location of the lines based on the centroid velocity fit to the summed N_2H^+ spectrum. Hyperfine components are indicated, along with their relative intensities expected for the optically thin case. As the figure clearly illustrates, many of the emission lines have high levels of self-absorption. We therefore focus primarily on the line fit parameters for the N_2H^+ and $H^{13}CO^+$ emission. Note that since there are seven N_2H^+ hyperfine components with different optical depths, the N_2H^+ line widths and centroids fit tend to be satisfactory, even if a small amount of self-absorption is present.

3. BASIC FILAMENT STRUCTURE: INTEGRATED INTENSITY

We first calculate the integrated intensity for the five molecular lines that do not exhibit self-absorption and hence are more likely to be optically thin to show the column density structure of the dense gas. The full MOPS bandwidths are very large (~ 200 km s^{-1}); in order to minimize the contribution of noise to the calculation, we restrict our integration to velocity channels close to where emission is expected. The velocity range is sufficient to extend slightly beyond the maximum observed line extent; the range adopted for each emission line is given in Table 1. The velocity centre for integration is,

in order of preference, as the signal to noise level allows: the centroid velocity fit to the particular line, the centroid velocity fit to the N_2H^+ line[10], or the approximate cloud-wide centroid velocity, 7.5 km s^{-1}. Figure 3 shows the integrated intensity maps for N_2H^+, $H^{13}CO^+$, and NH_2D, i.e., the brightest species without self-absorption, along with SiO, which lacks any clear detections. The typical uncertainty is given in Table 1.

Figure 3 shows that both the N_2H^+ and $H^{13}CO^+$ integrated intensities have a similar structure to that seen in dust emission. The integrated intensity for NH_2D is much fainter, but appears to follow a similar trend. All three of these molecular species are expected to be good tracers of dense gas (see, e.g., the discussion in Sanhueza et al 2012; Bergin & Tafalla 2007), which is confirmed by their good correspondence to the dust emission. $H^{13}CN$ (not shown in Figure 3) is also expected to be a good dense gas tracer (e.g., Hily-Blant et al 2010), however, our data has too poor a signal to noise level to see this definitively. Summing our data over many pixels shows hints that the central filament is brighter than the surrounding gas, although even this is only seen at a marginal level. The $H^{13}CN$ spectrum shown in Figure 2 is one of the brightest spectra resulting from summing the data over four by four pixels squared.

SiO is not detected with certainty anywhere in the map. As a tracer of shocked gas (see e.g., Caselli et al 1997, and references therein), its emission structure could be expected to differ from the other four species. The general lack of emission may indicate a lack of strong (highly supersonic) shocks, however, with the noise levels in our observations, we cannot rule out weaker shocks.

3.1. *Filament Geometry*

In Figures 1 and 3, differing filament shapes or geometries are visible north and south of the main cluster. The southern filament is dominated by a single nearly straight filament extending to the southeast, with several fainter filaments (e.g., pointing due south) apparent primarily in the dust emission map. In the north, however, the filamentary structure is more complex. A careful visual examination of both the dust emission and molecular data to the northwest of the main cluster shows a seemingly complex structure suggestive of overlap along the projected line of sight. Intertwined filaments have recently been identified through a careful analysis of the quiescent B213 filament in Taurus (Hacar et al in prep). Other observations of filaments, such as Orion (Johnstone & Bally 1999; Bally et al 1987) show morphologies suggestive of similar phenomena in higher-mass systems. Unlike B213, the large linewidths in the northern filament of Serpens South make the separation of velocity components difficult if not impossible, and for this paper, we restrict our analysis to the simpler southern filament.

We define the central or peak ridge of the southern filament by searching for the location of peak emission along every horizontal cut through the filament. For this detection, we use the dust continuum map; while the N_2H^+ integrated intensity map shows a similar distribution, the dust map has a higher signal to noise level. This filament

---

[10] N.B.: the N_2H^+ line is the brightest and most frequently detected of the five species without self-absorption.

definition is shown in Figure 4. For comparison, we also show a similar outline for the more complex northern filaments. For our analysis of the southern filament, we consider the data within $1'$ of the peak ridge (i.e., three $15''$ pixels on either side of the peak, or a diameter of 0.16 pc), and along a 0.33 pc extent. This area covers all of the strongest emission present in the southern filament and excludes any gas potentially associated with the much fainter filament to the west. Within this area, the southern filament has a mass of $\sim$20 $M_\odot$, based on the dust emission map[11]. Maury et al (2011) estimate a mass of 610 $M_\odot$ over a $15'$ by $25'$ area (i.e., several times larger than the entire extent of our Mopra observations), based on 1.2 mm MAMBO dust continuum data. For both our estimate and that in Maury et al (2011), a distance of 260 pc (e.g., Straižys et al 2003), is assumed, based on extinction estimates in the Aquila rift.

There is, however, some debate over the true distance to Serpens South. Recent VLBI measurements of a YSO in the Serpens main core suggest that the distance to Serpens main is roughly 415 pc (Dzib et al 2010). Complicating the picture is the fact that the gas velocities appear similar for Serpens main, Serpens South, and Aquila; see the discussion in Maury et al (2011) for more details. Since most existing analyses of Serpens South assume the closer distance of 260 pc (e.g., Gutermuth et al 2008; Maury et al 2011; Arzoumanian et al 2011), we also adopt that value here, but discuss in Section 7 how our results would differ if we instead assumed 415 pc.

4. GLOBAL VELOCITY GRADIENT

Figure 4 shows the centroid velocity fit to our N_2H^+ spectra (where the signal to noise ratio is 3.5 or more). A clear velocity gradient is visible along the southern filament (shown by the red dashed line), while the northern filaments have a structured, but more complex velocity field. If the southern filament is oriented with its southeast part further from us and the cluster centre closer to us, then an accelerating accretion flow would produce a velocity gradient similar to the one observed. The infall line profiles discussed in the next section lend further weight to this choice of filament orientation.

We measure the velocity gradient for the southern filament following the procedure outlined in Goodman et al (1993). We assume the N_2H^+ centroid velocities follow a simple linear form:

$$A\Delta\alpha + B\Delta\delta = C \qquad (1)$$

where $\Delta\alpha$ and $\Delta\delta$ are the changes in right ascension and declination across the map. We found the best-fitting values to the constants A and B using MPFIT (Markwardt 2008), and then converted all of the angular velocity gradients to physical scale assuming a distance of 260 pc. This yields an overall velocity gradient of 1.4 ± 0.2 km s^{-1}pc^{-1}, at an angle of $\sim 20°$ west of north. Note that while the $H^{13}CO^+$ centroid velocities (not shown) agree quite well with the N_2H^+ centroid velocities, fewer of the spectra have a signal to noise level

[11] We assume a temperature of 15 K and a dust opacity of 0.0114 cm^{2}g^{-1} (e.g. Enoch et al 2007); recent ammonia measurements suggest a dense gas temperature around 10-15 K in Serpens South, with the southern filament at $\sim$11-12 K further from the central cluster and $\sim$12-14K approaching the cluster (Friesen et al, in prep).

above 3.5, which leads to a less reliable measurement of the velocity gradient.

We can estimate the accretion rate implied by this velocity gradient by using a simple cylindrical model, shown in Figure 5. The cylinder has a mass M, length L, radius r, an inclination to the plane of the sky of angle α, and true motions of velocities $V_\parallel$ along the filament long axis, and $V_\perp$ infalling into the short axis (this final term will be of interest in the following section). The accretion rate, $\dot{M}_\parallel$, along the filament onto the central cluster is therefore the velocity along the filament times the density and the area perpendicular to the flow, or

$$\dot{M}_\parallel = V_\parallel \times \left(\frac{M}{\pi r^2 L}\right)(\pi r^2) \qquad (2)$$

which simplifies to $\dot{M}_\parallel = V_\parallel \frac{M}{L}$. Due to projection effects, we observe

$$L_{obs} = Lcos(\alpha) \quad \text{and} \quad V_{\parallel,obs} = V_\parallel \, sin(\alpha) \qquad (3)$$

with $V_{\parallel,obs} = \nabla V_{\parallel,obs} L_{obs}$. Therefore, the accretion rate is given by

$$\dot{M}_\parallel = \frac{\nabla V_{\parallel,obs} M}{tan(\alpha)} \qquad (4)$$

For the southern filament, we estimate a mass of 20.3 $M_\odot$ along a length of 0.33 pc and width of 0.08 pc (see Section 3.1), which corresponds to an accretion rate of 28 $M_\odot$ Myr^{-1} for $tan(\alpha) = 1$. Note that since we observe both a gradient along the filament and infall onto the filament (discussed in the next section), this already constrains α not to lie close to either of the possible extreme values ($0°$ for lying parallel to the plane of the sky and $90°$ for lying directly along the line of sight). We will furthermore show that the accretion rates estimated from both the motion along and across the filament are relatively high, which suggests that α is likely close enough to $45°$, so that the correction factor for each measure is only several times unity.

The velocity gradient used for the accretion rate estimate is also similar to values measured in other star-forming regions – for example, Bally et al (1987) find a gradient of $\sim$0.7 km s^{-1} pc^{-1} along several pc of the Orion integral shaped filament; Schneider et al (2010) find gradients of $\sim$0.8-2.3 km s^{-1} pc^{-1} along the DR21 filament, and Kirk et al (2010) find a general relationship in non-filamentary molecular gas structures between size and velocity gradient suggesting values around 1 km s^{-1} pc^{-1} for size scales of a few tenths of a parsec. The similarity of the measured gradient further suggests that projection effects are not extreme for the filament, if Serpens South is not atypical.

If the gradient were instead interpreted as rotation, then the total rotational energy would be

$$E_{rot} = \frac{1}{2}\left(\frac{ML^2}{3}\right)\left(\nabla V\right)^2 \qquad (5)$$

where the second term is the moment of inertia for a cylinder rotating longways around its end, and the final term represents the angular velocity squared. For the southern filament, this yields $E_{rot} \simeq 0.7$ $M_\odot$ km^2 s^{-2}. The gravitational binding energy is given by

$$E_{grav} = \frac{GMM_{clust}}{L} \qquad (6)$$

where M_{clust} is the mass of the central cluster, roughly 100 $M_\odot$, calculated in the same manner as the filament mass (see Section 3.1). Thus, the gravitational binding energy is a factor of more than ten higher, at $E_{grav} \simeq 26$ $M_\odot$ km^2 s^{-2}. With a freefall time of just ~ 0.3 Myr, several times less than the estimated age of the region, even if the filament was initially rotating, infall motions would rapidly dominate.

Finally, the velocity gradient *could* also be interpreted as outflow motion, if the orientation was the reverse of that assumed above. In this instance, stellar winds and outflows would be the most likely candidate source for driving the motions. Using a simple calculation to estimate the momentum and energy associated with such outflowing motions yields values of 9 $M_\odot$ km s^{-1} and 2 $M_\odot$ km^2 s^{-2} respectively. Nakamura et al (2011) estimate that the total momentum and energy in outflows (measured using CO(3-2) data) in Serpens South is ~ 8 $M_\odot$ km s^{-1} and ~ 65 $M_\odot$ km^2 s^{-1} respectively, with a total mass of outflowing material of only 0.6 $M_\odot$. While in principle, the YSO population could provide sufficient energy and momentum to drive the observed large-scale flow, the outflows observed by Nakamura et al (2011) are multi-directional, not highly collimated, as would be required.

5. INFALL ALONG THE LINE OF SIGHT

We next utilize information from an optically thick line showing self-absorption to measure gas accretion across (i.e., building up additional mass onto) the filament. In the classic case of two converging layers, the gas is assumed to have an increasing excitation temperature toward the centre (where the density is also higher); self-absorption in optically thick lines occurs for the emission originating from the furthest pieces of gas at any given velocity. Therefore, emission from the (blue-shifted) layer moving toward the observer is emitted primarily from the higher excitation, denser part of the slab, while the reverse is true for the (red-shifted) layer moving away from the observer (e.g. Myers et al 1996). Infall profiles therefore show brighter peaks blue-ward of the peak emission of an optically thin line, with a lower red shoulder, and sometimes a central dip. Using simplified assumptions about the gas properties, the emission profile of a line showing such a red-blue asymmetry can be used to estimate a characteristic infall velocity of the gas (e.g., Evans 1999; Myers et al 2000).

In Serpens South, we observe self-absorption in several of our emission lines: HCO$^+$, HCN, and HNC. Of these lines, the HNC is the least self-absorbed, and therefore is the brightest and has the highest signal to noise level. A high signal to noise level is required to obtain reasonable model fits to infall spectra – deVries & Myers (2005) find signal to noise levels > 30 are required for good results. In order to further maximize our signal to noise level, we therefore spatially average spectra along the southern filament. As discussed in the previous section, there is a global velocity gradient running along the southern filament, which needs to be accounted for prior to averaging. We use the N$_2$H$^+$ centroid velocities fit at each pixel to first shift all of the HNC spectra to a common velocity centre prior to averaging, again considering spectra within 1' (or 3 pixels on either side) of the filament's peak ridge identified. Figure 6 shows

the result of this summation for HNC, as well as for the two optically thin lines, N$_2$H$^+$ and H^{13}CO$^+$. In the case of N$_2$H$^+$, only the isolated component is shown for simplicity. The HNC spectrum shows a brighter blue and fainter red peak with strong central dip around the peak emission of N$_2$H$^+$ and H^{13}CO$^+$, in agreement with expectations for infall. The HNC(1–0) transition does have hyperfine structure, however, this is on a much smaller scale than the infall profile seen, as shown in the right hand panel of Figure 6.

We estimate the infall velocity using the Hill5 model (and line fitting code) described in deVries & Myers (2005). The Hill5 model considers gas with a linearly increasing excitation temperature toward the centre, with each half of the gas moving toward the other at a fixed velocity. In their analysis, deVries & Myers (2005) found that the Hill5 model tended to provide the best fit to a range of both simulated and real spectra with infall motions; the inclusion of an increase in the excitation temperature allowed for much better match than the classic two-slab model of Myers et al (1996). The variables in the Hill5 model are the infall velocity, V_{in}, the (Gaussian sigma) velocity dispersion, δV, total optical depth, τ, system velocity V_{lsr}, and peak excitation temperature, T_{peak}. Note that the system velocity is expected to be 0 in our case, since the individual HNC spectra were all shifted by the N$_2$H$^+$ centroid velocity fit at the same pixel prior to the summation. Using the Hill5 model, we find the best-fitting parameters listed in Table 2 under 'Fit-1'.

In order to estimate the fitting errors, we ran the fitter on 1000 realizations of the spectrum with random noise added at the same level as observed[12]. This test yielded several unexpected results. In a small number of cases (26 of 1000), the 'best' fit clearly got 'stuck' in a local minimum of χ^2 space, with unphysical parameters (optical depths in excess of 20 and peak excitation temperatures often around several hundred). These models provided visually poor fits to the spectra, and so we discarded these cases. These fits likely could have been fixed by modifying the fitting tolerances in the Hill5 fitter, but this seemed unnecessary, given the small overall number. Of the remaining 974 fits to the data plus random noise, 686 were found to have values clustered very close to the original fit (these were used to calculate the formal errors in 'Fit-1'), while the remaining 288 were clustered around a different set of fit parameters, listed under 'Fit-2' in Table 2. Visually, this other set of fits also are a reasonable match to the data, and the distribution of χ^2 values are similar for both sets of fits. Therefore, these second fit parameters appear to be a viable second solution to the best-fitting Hill5 model, using only the information available from the HNC spectrum.

We use the additional information available from the optically thin spectra (H^{13}CO$^+$ and possibly N$_2$H$^+$) to argue that Fit-1 best matches the full suite of data. We calculate the corresponding optically thin spectra for both Fit-1 and Fit-2, using the fitted parameters but a lower optical depth. For Fit-2, the optically thin spectrum predicted has two distinct velocity components separated by more than the linewidth. Effectively, Fit-2

---

[12] Note that this increases the total noise in the spectrum by a factor of $\sqrt{2}$.

represents a model of two independent layers of material moving toward each other. As shown in Figure 6, two distinct velocity components are not observed in either of the brightest optically thin tracers, i.e., the N_2H^+ isolated hyperfine component or $H^{13}CO^+$. This implies that Fit-1 is the most consistent with the observations.

We ran several simple tests with the online non-LTE radiative transfer calculator, Radex[13] (Van der Tak et al 2007) to check that the fitted values are reasonable. We assume an HNC abundance of 6×10^{-10} typical of dense core gas (Hily-Blant et al 2010), and adopt gas properties (density, column density, temperature, total velocity dispersion) based on the observations discussed earlier. The predicted optical depth ranges from roughly 6 to 8, for temperatures (and the associated derived densities and column densities) between 12 and 15 K. Given that a cold dense core HNC abundance is likely an overestimate for a filament, and the uncertainties in various parameters used to estimate the density and column density from the dust maps, the Hill5 model fit of an optical depth of 2.7 for 'Fit-1' is in reasonable agreement; the optical depth of 1.6 from 'Fit-2' is less consistent with the observational expectations.

Using the same toy model as shown in Figure 5, the accretion rate onto the filament can be estimated from the above infall velocity, i.e., the velocity onto the filament times the density and filament surface area of the short axes, or

$$\dot{M}_\perp = V_\perp \times \left(\frac{M}{\pi r^2 L}\right)(2\pi r L) \qquad (7)$$

which simplifies to $\dot{M}_\perp = 2V_\perp \frac{M}{r}$. Due to projection effects, we observe

$$V_{in} = V_\perp cos(\alpha) \qquad (8)$$

while the observed filament radius / short axis should be invariant under rotation. Therefore, the accretion rate onto the filament is given by

$$\dot{M}_\perp = \frac{2V_{in}M}{rcos(\alpha)} \qquad (9)$$

This corresponds to an accretion rate of 130 $M_\odot$ Myr^{-1} for $cos(\alpha) = 1$ and is therefore a lower limit to the true rate. Additionally, the infall velocity fit with the Hill5 model is expected to be a lower limit to the true characteristic infall speed: the infall was modelled as two infalling parallel slabs, while in a cylindrical geometry, some of the inward motions will appear smaller along the line of sight. Finally, note that using the alternative V_{in} of 0.54 km s^{-1} from Fit-2 corresponds instead to a lower limit of ~ 280 $M_\odot$ Myr^{-1}.

Both the accretion rate onto the filament and from the filament onto the cluster, without accounting for projection effects, are within a factor of a few of the star formation rate in the cluster estimated by Gutermuth et al (2009), and somewhat larger than the rate estimated by Maury et al (2011). Any correction for projection effects made to the accretion onto the filament will serve to further increase that estimate, i.e., beyond 130 $M_\odot$ Myr^{-1}, while the accretion rate from the filament onto the

cluster could be larger or smaller than our estimated 28 $M_\odot$ Myr^{-1} after correcting for projection.

If the filament were projected at an angle of 30 to 60 degrees relative to the plane of the sky, then the accretion onto the central cluster measured would be within a factor of 0.6 to 1.7 of its true value, while the accretion onto the filament measured would be a factor of 1.15 to 2 of its true value. Based on the combination of filament appearance, velocities measured, and accretion rates derived, we believe that $30° \leq \alpha \leq 60°$ is a reasonable range of filament angles.

5.1. *Other Lines*

In addition to the self-absorbed HNC emission, both HCO^+ and all three hyperfine components of HCN also show signs of self-absorption. We performed the same spectral averaging across the southern filament for these emission lines as described for HNC. We additionally shift each HCN (and associated $H^{13}CN$) hyperfine component to the velocity it would have if it were the sole emission line. Figure 7 shows the resulting spectral line profiles. As can be easily seen from the figure, all four of the optically thick lines show such strong self-absorption that relatively little emission is seen. We attempted to model the emission lines with a Hill5 (or other) profile, but due to the low signal to noise, even with averaging over the filament, we were unsuccessful.

The degree of self-absorption in HCO^+ and HCN is surprisingly large – the HCO^+ emission peaks at only half the value of the $H^{13}CO^+$ peak, whereas in an optically thin environment, the ratio would be somewhere around a factor of 40 (for non PDR molecular clouds at a galactocentric separation, similar to the Sun, of 8 kpc; Savage et al 2002). In $H^{13}CN$, the line ratios for optically thin gas would be 1:5:3 (for the top right, bottom left, and bottom right panels in Figure 7), whereas HCN is clearly brightest in the (F=0–1) or first / leftmost hyperfine component. This would be consistent with a picture wherein the highest levels of self-absorption occur in the optically thickest components, and the least in the optically thinnest.

Recent work suggests that the rate coefficients for HCN and HNC differ significantly (Dumouchel et al 2010), implying sensitivity to different density ranges of material, and thus explaining why the two do not show similar levels of self-absorption. Alternatively, studies have shown that hyperfine anomalies in HCN(1–0) are relatively common in higher column density environments, and tend to lead to precisely the trend in peak brightnesses observed (Loughnane et al 2012). The $H^{13}CN$ emission is extremely faint, but appears to be roughly consistent with optically thin emission with the predicted line strengths (with no significant emission detected in the first / leftmost / F=0–1 component), this is also consistent with the hyperfine anomaly study of Loughnane et al (2012), who find that $H^{13}CN$ does not have anomalous ratios in sources where HCN does.

We ran several additional checks to ensure that these severely self-absorbed spectra are real, and were not affected by any systematic effects. For the velocity centroids, all eight molecules were observed simultaneously with MOPS, suggesting that any error with either the measured line velocities, or the adopted central frequencies of each molecule, would have to be present in all

---

[13] Radex is available at http://home.strw.leidenuniv.nl/-~moldata/radex.html.

of our observations. The Serpens South data presented here are part of a larger project which includes four other embedded cluster-forming regions. Examining our data in the other four regions shows very good agreement between the different molecular line centroid velocities where there is optically thin emission, suggesting that there are no systematic effects with our velocity scale. Similarly, the peak line emission in these other regions, and the relative values of peak intensity, agree well with expectations, suggesting no systematic effects there either. Finally, we note that similarly severely self-absorbed emission line profiles showing a complete absence of a red shoulder have also been observed in Serpens South with a different telescope and molecular line transition. CO(3-2) emission observed with the ASTE 10 m telescope show a similarly shaped profile in some areas of the cluster (see, e.g., the bottom panels in Figure 6 of Nakamura et al 2011).

6. COLUMN DENSITY PROFILE

6.1. *Mass per Unit Length*

In this section, we examine some basic properties of the column density structure of the southern filament. The simplest property which can be measured for filaments is their mass per unit length. Assuming that a filament can be approximated as an infinitely extended, self-gravitating, isothermal cylinder with no magnetic support, then the maximum mass per unit length which can be in equilibrium is

$$M_{line,crit} = 2c_s^2/G \qquad (10)$$

$$M_{line,crit} = 16.7\Big(\frac{T}{10\ K}\Big)\ M_\odot\ pc^{-1} \qquad (11)$$

(e.g., Ostriker 1964; Inutsuka & Miyama 1997). Observations of the ammonia (1,1) and (2,2) inversion transitions (Friesen et al, in prep) indicate that the kinetic temperature across Serpens South is in the range of 10 to 15 K, implying $M_{line,crit}$ is between 17 and 25 $M_\odot$ pc^{-1}. If the observed non-thermal motions were also considered to contribute to supporting the filament (e.g., Fiege & Pudritz 2000a; Miettinen 2012), then with a typical velocity dispersion of ~ 0.36 km s^{-1} (Gaussian sigma units) for N_2H^+ (mean or median value over the southern filament), then $M_{line,crit}$ is roughly 80 $M_\odot$ pc^{-1}.

In the southern filament, we find a mass of 20.3 $M_\odot$ along 0.33 pc, implying $M_{line} = 62$ $M_\odot$ pc^{-1}, i.e., several times the critical value, unless all of the non-thermal motion is contributing thermal-like support. The total amount of support available is therefore likely insufficient to keep the filament in equilibrium, implying that it should be radially contracting. Supercriticality is consistent with our velocity measurements showing that gas is globally infalling in the filament. Arzoumanian et al (2011) similarly find that filaments with higher column densities, such as in Aquila, tend to have supercritical values of M_{line}. Filaments associated with massive star formation tend to be highly supercritical with M_{line} often ten times larger than that in nearby regions (Hennemann et al 2012).

6.2. *Radial Column Density Profile*

In this section, we analyze the radial column density profile of the filament using the millimetre continuum emission. We use the peak ridge of the filament discussed in Section 3, and for each pixel in the original AzTEC/ASTE data, we measure the column density profile along lines of constant declination. This provides for more regular and better sampling than to measure points perpendicular to the local filament orientation; we later correct our radial separation measurements to account for an average filament angle of 45°.

All ground-based (sub)millimetre measurements are insensitive to the largest scale structures, due to the observing methods which must be employed. For the AzTEC/ASTE map we analyze, Gutermuth et al (in prep) have devised a novel technique which is able to recover flux out to about 5′, a much larger scale than is typical. In summary, the technique iteratively subtracts a model of the astronomical signal from the bolometer timestream data and then recomputes the atmospheric filtering and regenerates the signal model map. The initial model is just the base pipeline-produced map masked to a signal to noise of 2, and convergence of the process is achieved when no new signal is found in an iteration down to a signal to noise of 3. Despite this marked improvement in map reconstruction, the very largest-scale structures with shallow or flat radial column density profiles will not be included in the map. Some amount of large-scale structure is expected to be present, as Serpens South is coincident with a roughly degree wide overdensity of dust extending to the well-known W40 active star-forming region. The 2MASS-based dust extinction map of Rowles & Froebrich (2009)[14] show that visual extinctions in excess of 5 to 10 mag are common across this area. Some, but not all, of this extinction undoubtedly represents diffuse material unassociated with the individual star-forming regions like Serpens South. Any material that is associated with Serpens South, however, would effectively result in a missing linear offset to the derived column density profile; the Serpens South filament is sufficiently compact that the *shape* of the column density profile should be correct. The function we fit to the column density profile is dependent on absolute values, not just the shape, so we limit our analysis to column densities where the fractional errors due to any missed large-scale structure are reasonable. If a constant background of $A_V = 1$ mag is missing from the AzTEC/ASTE map, there would be a $\leq 30\%$ underestimate of the inferred column density at fluxes of 0.067 Jy bm^{-1}; we adopt this as our lower limit. An additional complication to the analysis arises from a second, fainter filament to the west of the one we analyze. In order to prevent this structure from confusing the radial column density profile, we additionally exclude pixels which lie westward of the minimum value between the two filaments.

After measuring the radial column density profile along the entire peak ridge, we calculate the mean and standard deviation at each radial separation, similar to Arzoumanian et al (2011). The mean profile and standard deviation of the column density profile of the southern filament is shown in Figure 8. For comparison, the

---

[14] These maps are available at http://astro.kent.ac.uk/extinction.

dotted red line shows the ASTE beam; clearly the filament is resolved.

We compare the filament column density profile to the same suite of models as in Arzoumanian et al (2011):

$$\Sigma_p(r) = A_p \frac{\rho_c R_{flat}}{[1 + (r/R_{flat})^2]^{\frac{p-1}{2}}} \qquad (12)$$

where Σ_p is the column density at radial separation r, ρ_c is the central (mass) density, R_{flat} characterizes the inner flat part of the profile, and

$$A_p = \frac{1}{cosi} \int_{-\infty}^{\infty} \frac{du}{(1+u^2)^{p/2}} \qquad (13)$$

is a constant, and the inclination angle along the line of sight, i, is assumed to be 0 for simplicity.

Assuming that the observed column density profile is additionally convolved with the ASTE beamsize, we use the MPFIT minimization code (Markwardt 2008) to determine the best fitting parameters. Allowing all three free parameters to vary, we find $\rho_c = 3.6 \pm 2.2 \times 10^5$ cm^{-3}, $R_{flat} = 0.010 \pm 0.006$ pc, and $p = 1.9 \pm 0.2$. Our values for R_{flat} and p lie within the range found by Arzoumanian et al (2011) for all filaments within the Aquila Rift (note their ρ_c values were not published), including a power law index which is shallower than for an isothermal cylinder. It is important to note, however, that unlike Arzoumanian et al (2011), we are not able to make a strong a statement on the power law index of the filament. The restrictions discussed above on where we are able to measure the radial column density profile limit our analysis to relatively close to the central ridge. Arzoumanian et al's comparable radial column density profile extends a factor of nearly 30 larger in radius than ours. With the relatively small range in radial separations, our ability to constrain the power law index is weak. Figure 8 shows also the best fit obtained using a power law index of 4 (corresponding to an isothermal cylinder), demonstrating that an isothermal model also can provide a reasonable fit to our data. The temperature required for the isothermal fit is 43 K, which is similar to the temperature implied by the nonthermal velocity dispersion in N$_2$H$^+$ (around 50 K for $\sigma = 0.36$ km s^{-1}). This is consistent with Section 6.1 where we showed that thermal pressure was insufficient to balance the gravity.

Recently, Juvela et al (2012) created synthetic observations of filaments formed in turbulent simulations, to investigate the effect of instrumental noise and changing dust properties on the inferred filament column density profile and mass per unit length, especially as relates to *Herschel* data. They find that the mass per unit length is reasonably robust to these uncertainties, while the parameters fit to the filament column density profile can be more uncertain in cases of higher noise / poorer resolution or a dust opacity which varies with density.

7. DISCUSSION

The southern filament in Serpens South has similar column density properties to star-forming filaments recently studied with *Herschel* (Arzoumanian et al 2011), with a mass per unit length several times larger than the critical value for thermal support, and a radial column density profile which is consistent with $p \sim 1.5 - 2.5$.

In fact, the Serpens South filament is included in the Arzoumanian et al (2011) sample of 'Aquila' filaments, although the individual filament locations / properties are not given in their paper to allow a more detailed comparison. The relatively large velocity dispersions seen in dense gas tracers in the southern filament could be interpreted as evidence for providing sufficient stability against gravitational collapse, however, our more detailed kinematic analysis suggests that the filament is in fact not in equilibrium. We find evidence for mass flows both along the filament onto the central cluster and onto the filament from the less dense surroundings, with accretion rates of order 28 and 130 M$_\odot$ Myr^{-1} respectively. These rates are uncertain by a factor of a few, for several reasons, including the angle of the filament with respect to the plane of the sky.

Although both accretion rates are uncertain to a factor of a few, it appears likely that the accretion rate onto the filament is larger than the accretion rate from the filament onto the central cluster. Formally, in order to have the latter rate be higher, the filament angle would need to satisfy

$$\frac{28 \ M_\odot \ Myr^{-1}}{tan(\alpha)} \geq \frac{130 \ M_\odot \ Myr^{-1}}{cos(\alpha)} \qquad (14)$$

which is satisfied for $\alpha \leq 12°$, i.e., a filament which is nearly parallel to the plane of the sky. Such a small inclination angle seems unlikely, but note that uncertainties in all observed quantities (mass, radius, velocity gradient, and infall velocity) could allow for a slightly larger range of angles. One must always use caution in interpreting velocity measures from different molecular tracers. The gas velocity could be some (non-constant) function of density, and using different molecular tracers for each accretion rate measure could in principle reflect that, rather than overall flow differences in the two directions. The only way to circumvent this potential issue entirely would be to use observations of a single self-absorbed molecule and its rarer isotopologue for both measures. We do not have such data available at high enough signal to noise, however, the consistency of the HNC self-absorption dip with the N$_2$H$^+$ and H^{13}CO$^+$ peak emission suggests all are tracing similar volumes of gas, and that this should not be a major problem.

If the tentative difference in accretion rates is true, this could imply that in the future, the accretion rate onto the central cluster will also increase (given the larger amount of mass available in the filament), and thus lead to more vigorous star formation in the cluster centre. It is also possible that the increase in mass in the filament could promote local instabilities in the filament, leading to core formation, and eventually to a series of star formation sites along the filament. Dense cores are, in fact, already observed in the AzTEC/ASTE data along the filament, as well as in 8 μm absorption. A small number of class 0 and I YSOs are also seen, which may be an indication of past instabilities in the filament. The small cluster of class II YSOs just past the southern end of the southern filament suggests a previous episode of star formation, perhaps also associated with the filament.

At the current estimated accretion rate of 28 M$_\odot$ Myr^{-1}, the cluster's membership would roughly double in 1 Myr with the addition of about 60

YSOs, assuming a mean mass of 0.5 M$_\odot$. An increasing accretion rate would lead to a larger number of YSOs. From these estimates, we can see that our estimated accretion rate from the filament onto the cluster is at a comparable level to previous observational estimates of the rate of mass supply required to form the current generation of YSOs in the cluster centre. We can therefore conclude that filamentary accretion is an important, if not the dominant, factor in governing the formation and evolution of stars in the central cluster.

Throughout this analysis, we have adopted a distance to Serpens South of 260 pc (e.g., Straižys et al 2003), for consistency with previous work, although recent VLBI observations suggest that a distance of $\sim$ 415 pc (Dzib et al 2010) applies to at least the main Serpens cluster. If this distance is also appropriate for Serpens South, then the quantities we estimate in our analysis here become a factor of several larger. The mass in the southern filament would increase by a factor of 2.5, the velocity gradient would decrease by a factor of 1.6, and all other quantities of interest (lengths, accretion rates, mass per unit length) increase by a factor of 1.6; the accretion rates become 45 M$_\odot$ Myr^{-1} parallel to the filament (onto the cluster) and 208 M$_\odot$ Myr^{-1} perpendicular to the filament. None of these changes effect our conclusions qualitatively, and in fact, they tend to strengthen our finding that filamentary accretion is important in Serpens South.

Filament-cluster systems such as Serpens South present a unique opportunity to gain a deeper understanding of cluster formation. With more sensitive observations, it should be possible to measure the spatial variation in the infall velocity across the filament, which could be used to model the full 3D velocity profile of material in the filament. This in turn can provide a straightforward test of the relative importance of magnetic fields, gravity, and turbulence in the ongoing cluster accretion, as discussed in Balsara et al (2001) and Heitsch (in prep).

8. CONCLUSION

Using a combination of dust column density information derived from AzTEC/ASTE continuum maps (Gutermuth et al, in prep) and dense gas kinematics derived from Mopra spectral maps, we study the flow of gas along the southern filament of the Serpens South embedded cluster. We find that the filament appears typical in terms of column density properties (e.g., a supercritical mass per unit length). The multiple molecular emission lines observed in our Mopra survey allow us to infer the possible presence of an accretion flow from the filament onto the central cluster (if the filament is in front of the cluster), and additionally we find that material continues to be accreted onto the filament. We estimate accretion rates of 28 M$_\odot$ Myr^{-1} for accretion onto the central cluster, and a lower limit of 130 M$_\odot$ Myr^{-1} for infall onto the filament (assuming a distance to Serpens South of 260 pc). Both of these are similar in magnitude to the estimated current rate of star formation in the central cluster.

Filamentary accretion flows therefore appear to be an important mechanism for supplying the material necessary to form the YSOs in this cluster. As more embedded clusters and their associated filaments are identified in current surveys, it will be interesting to measure the associated gas kinematics to determine whether other embedded clusters behave similarly to Serpens South.

REFERENCES

Ahrens, V., Lewen, F., Takano, S., Winnewisser, G., Urban, S., Negirev, A. A., & Koroliev, A. N. 2002, Z. Naturforsch. 571, 669

André, Ph. et al 2010, A&A, 518, L102

Arzoumanian, D., et al. 2011, A&A, 529L, 6

Bally, J., Lanber, W. D., Stark, A. A., & Wilson, R. W. 1987, ApJ, 312L, 45

Balsara, D., Ward-Thompson, D., & Crutcher, R. M. 2001, MNRAS, 327, 715

Bechtel, H. A., Steeves, A. H., & Field, R. W. 2006, ApJ, 649, 53

Bergin, E. A. & Tafalla, M. 2007, ARA&A, 45, 339

Bester, M., Yamada, K., Winnewisser, G., & Urban, S. 1983, A&A, 121L, 13

Bressert, E., Bastian, N., Gutermuth, R., et al 2010, MNRAS, 409L, 54

Caselli, P., Hartquist, T. W., & Havnes, O. 1997, A&A, 322, 296

deVries, C. H. & Myers, P. C. 2005, ApJ, 620, 815

Dobashi, K., Yonekura, Y., Mizuno, A., & Fukui, Y. 1992, AJ, 104, 152

Dumouchel, F., Faure, A., & Lique, F. 2012, MNRAS, 406, 2488

Dzib, S., Loinard, L., Mioduszewski, A. J., Boden, A. F., Rodríguez, L. F., & Torres, R. M. 2010, ApJ, 718, 610

Enoch, M. L., Glenn, J., Evans, N. J. II, Sargent, A. I., Young, K. E., & Huard, T. L. 2007, ApJ, 666, 982

Evans, N. J. II 1999, ARA&A, 37, 311

Fiege, J. D. & Pudritz, R. E. 2000, MNRAS, 311, 85

Goodman, A. A., Benson, P. J., Fuller, G. A., & Myers, P. C. 1993, ApJ, 406, 528

Gutermuth, R. A. et al 2008, ApJ, 673, 151

Gutermuth, R. A., Megeath, S. T., Myers, P. C., Allen, L. E., Pipher, J. L., Fazio, G. G. 2009, ApJS, 184, 18

Hacar, A. & Tafalla, M. 2011, A&A, 533, 34

Hennemann, M. et al 2012, A&A, 543, 3

Hily-Blant, P., Walmsley, M., Pineau Des Forêts, G., & Flower, D. 2010, A&A, 513, 41

Inutsuka, S-I. & Miyama, S. M. 1997, ApJ, 480, 681

Johnstone, D. & Bally, J. 1999, ApJ, 510, L49

Juvela, M., Malinen, J., & Lunttila, T. 2012, A&A accepted (arXiv:1207.3635)

Kirk, H., Pineda, J. E., Johnstone, D., & Goodman, A. 2010, ApJ, 723, 457

Lada, C. J. & Lada, E. A. 2003, ARA&A 41, 57

Ladd, N., Purcell, C., Wong, T., & Robertson, S. 2005, PASA, 22, 62

Loughnane, R. M., Redman, M. P., Thompson, M. A., Lo, N., O'Dwyer, B., & Cunningham, M. R. 2012, MNRAS, 420, 1367

Lovas, F. J., Bass, J. E., Dragoset, R. A., & Olsen, K. J. 2009, NIST Recommended Rest Frequencies for Observed Interstellar Molecular Microwave Transitions - 2009 Revision (version 3.0) Available at http://physics.nist.gov/restfreq. National Institute of Standards and Technology, Gaithersburg, MD

McCutcheon, W. H., Roger, R. S., & Dickman, R. L. 1982, ApJ, 256, 139

Manson, E. L. Jr, Clark, W. W., DeLucia, F. C., & Gordy, W. 1977, Phys. Rev., 15A, 223

Markwardt, C. B. 2008 in Astronomical Society of the Pacific Conference Series, Vol 411, proc. Astronomical Data Analysis Software and Systems XVIII, eds. D. Bohlender, P. Dowler & D. Durand (ASP: San Francisco), pp 251

Maury, A. J., André, P., Men'shchikov, A., Könyves, V., & Bontemps, S. 2011, A&A, 535, 77

Miettinen, O. 2012, A&A, 540, 104

Müller, H. S. P., Schlöder, F., Stutzki, J., & Winnewisser, G. 2005, J. Mol. Struct, 742, 215

Myers, P. C., Mardones, D., Tafalla, M., Williams, J. P., & Wilner, D. J. 1996, ApJ, 465, L133

Myers, P. C., Evans, N. J. II, & Ohashi, N. 2000 in Protostars and Planets IV, eds Mannings, V., Boss, A. P., & Russell, S. S. (University of Arizona Press: Tucson), pp 217

Myers, P. C. 2009, ApJ, 700, 1609

Myers, P. C. 2011, ApJ, 735, 82

Nakamura, F., et al. 2011, ApJ, 737, 56

Ostriker, J. 1964, ApJ, 140, 1056

Pagani, L., Daniel, F., & Dubernet, M.-L. 2009, A&A, 494, 719

Pearson, E. F., Creswell, R. A., Winnewisser, M., & Winnewisser, G. 1976, Z. Naturforsch., 31a, 1394

Rosolowsky, E. W., Pineda, J. E., Foster, J. B., Borkin, M. A., Kauffmann, J., Caselli, P., Myers, P. C., & Goodman, A. A. 2008, ApJS, 175, 509

Rowles, J. & Froebrich, D. 2009, MNRAS, 395, 1640

Sanhueza, P., Jackson, J. M., Foster, J. B., Garay, G., Silva, A., & Finn, S. C. 2012, ApJ accepted

Savage, C., Apponi, A. J., Ziurys, L. M., Wyckoff, S. 2002, ApJ, 578, 211

Schmid-Burgk, J., Muders, D., Mü ller, H. S. P.,& Brupbacher-Gatehouse, B. 2004, A&A, 419, 949

Schneider, N., Csengeri, T., Bontemps, S., Motte, F., Simon, R., Hennebelle, P., Federrath, C., & Klessen, R. 2010, A&A, 520, 49

Smith, R. J., Longmore, S., & Bonnell, I. 2009, MNRAS, 400, 1775

Straižys, V., Černis, K., & Bartašiūtè 2003, A&A, 405, 585

Sugitani, K., et al. 2011, ApJ, 734, 63

Uchida, Y., Mizuno, A., Nozawa, S., & Fukui, Y. 1990, PASJ, 42, 69

Ulich, B. L. & Haas, R. W. 1976, ApJS, 30, 247

Van der Tak, F. F. S., Black, J. H., Schöier, F. L., Janser, D. J., & van Dishoek, E. F. 2007, A&A, 468, 627

Vasyunina, T., Linz, H., Henning, Th., Zinchenko, I., Beuther, H., & Voronkov, M. 2011, A&A, 527, 88

Wilson, G. W. et al. 2008, MNRAS, 386, 807

Winston, E. et al. 2010, AJ, 140, 266

Table 1
Basic Line Properties

Molecule	Frequency (MHz)	HF component[a] (if applicable)	Ref.[b]	Int. Range[c] (km s^{-1})	Integrated Noise[d] (K km s^{-1})
N_2H^+(1–0)	93173.4669	$F_1, F = 2 - 1, 2 - 1$	1	-10.5→7.5	4.38
$H^{13}CN$(1–0)	86340.1840	$F = 2 - 1$	2	-8.5→6.5	3.87
HCN(1–0)	88631.8473	$F = 2 - 1$	3	-9→7	4.02
HNC(1–0)	90663.5560	$F = 2 - 1$	4	-2→2	2.04
$H^{13}CO^+$(1–0)	86754.2884	N/A	5[e]	-2→2	2.02
HCO^+(1–0)	89188.5260	N/A	6	-5→5	3.23
SiO(2–1)	86846.9600	N/A	7	-1.5→1.5	1.76
NH_2D(1,1)	85926.2630	N/A	8	-6.5→6.5	3.66

[a] In the case of a species with hyperfine splitting, the transition used for centering.
[b] Reference for the adopted frequency: 1. Pagani et al (2009); 2. Pearson et al (1976), as recommended by JPL (`http://spec.jpl.nasa.gov`); 3. Ahrens et al (2002), as recommended by CDMS (Müller et al 2005); 4. Bechtel et al (2006); 5. Schmid-Burgk et al (2004), as recommended by CDMS; 6. Ulich & Haas (1976), as recommended by NIST (Lovas et al 2009) 7. Manson et al (1977), as recommended by CDMS; 8. Main frequency listed for no hyperfine splitting from Bester et al (1983), as recommended by NIST (our sensitivity is too low to pick up the satellite components).
[c] The range in velocities, relative to the line centroid, used when calculating the integrated intensity.
[d] The median formal 1-sigma error on the integrated intensity in brightness temperature units, i.e., the typical spectral rms multipled by the square root of the number of spectral channels integrated over.
[e] Note that hyperfine splitting was detected by Schmid-Burgk04, but with the components separated by only 0.133 km s^{-1}, this would not be visible in our Mopra data.

Table 2
Hill5 Model Parameters Fit to HNC

Fit[a]	V_{infall}[b] (km s^{-1})	δV[b] (km s^{-1})	V_{lsr}[b] (km s^{-1})	τ[b]	T_{peak}[b] (K)
Fit-1	0.25±0.02	0.45 ±0.01	0.05±0.01	2.7±0.1	6.33±0.06
Fit-2	0.54±0.01	0.36 ±0.01	0.06±0.01	1.6±0.1	6.6±0.1

[a] In our 1000 randomized fits, two clusters of fit parameters were identified, as listed here. The original HNC fitted Hill5 parameters are all identical to the mean values listed for Fit-1.
[b] Mean and standard deviations of the infall velocity, velocity dispersion (Gaussian sigma units), centroid velocity, optical depth, and peak excitation temperature, for the subset of the 1000 randomized trials.
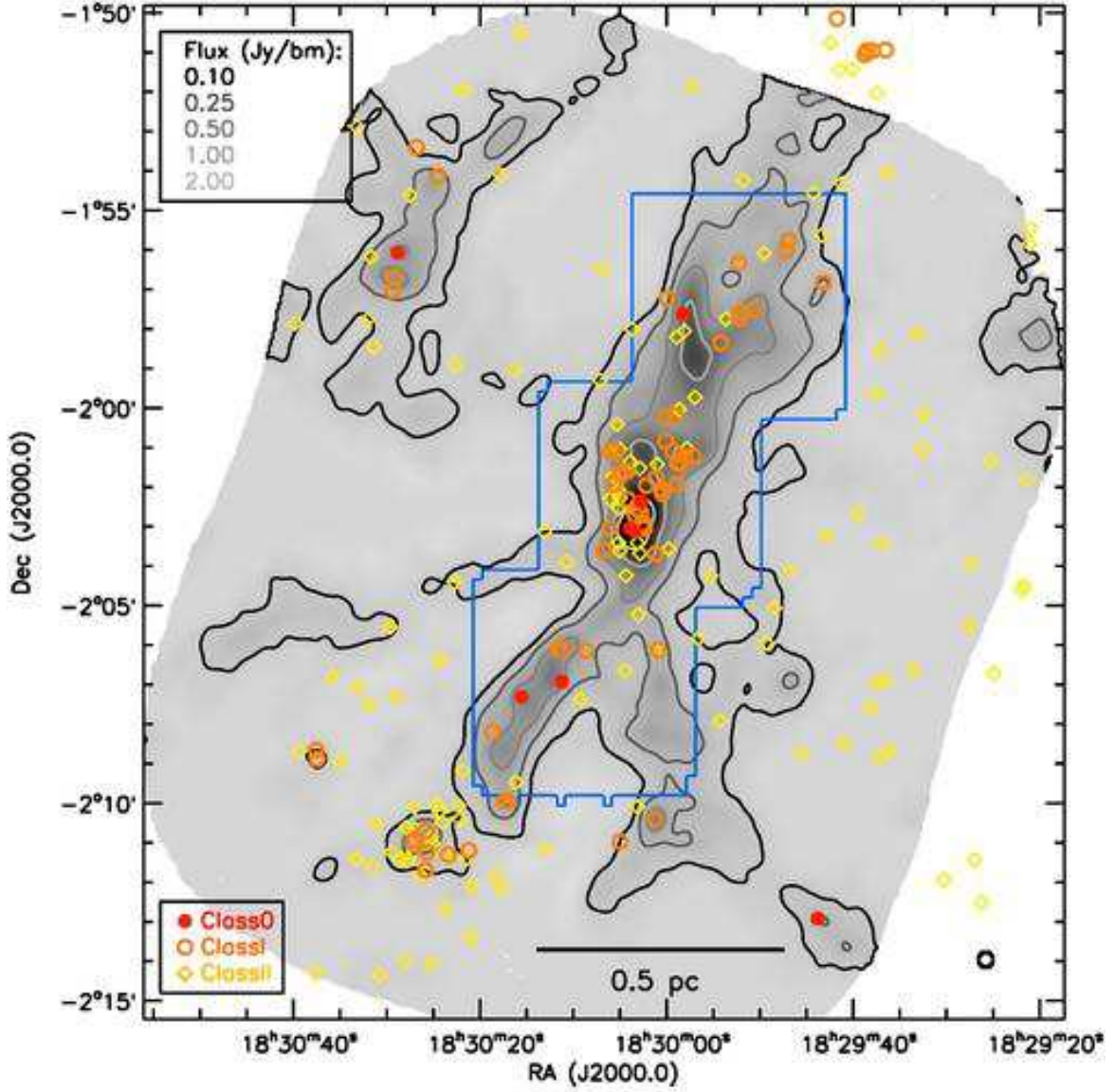
Figure 1. The large-scale context of our Mopra observations of Serpens South. The greyscale image and contours show an AzTEC/ASTE map of the millimetre dust continuum emission, while the red filled circles, orange open circles, and yellow diamonds show the YSO population found in *Spitzer* data. The black circle at the bottom right corner shows the AzTEC/ASTE beamsize (28″ FWHM). The blue contour shows the region mapped with Mopra, covering all of the main filamentary structure.
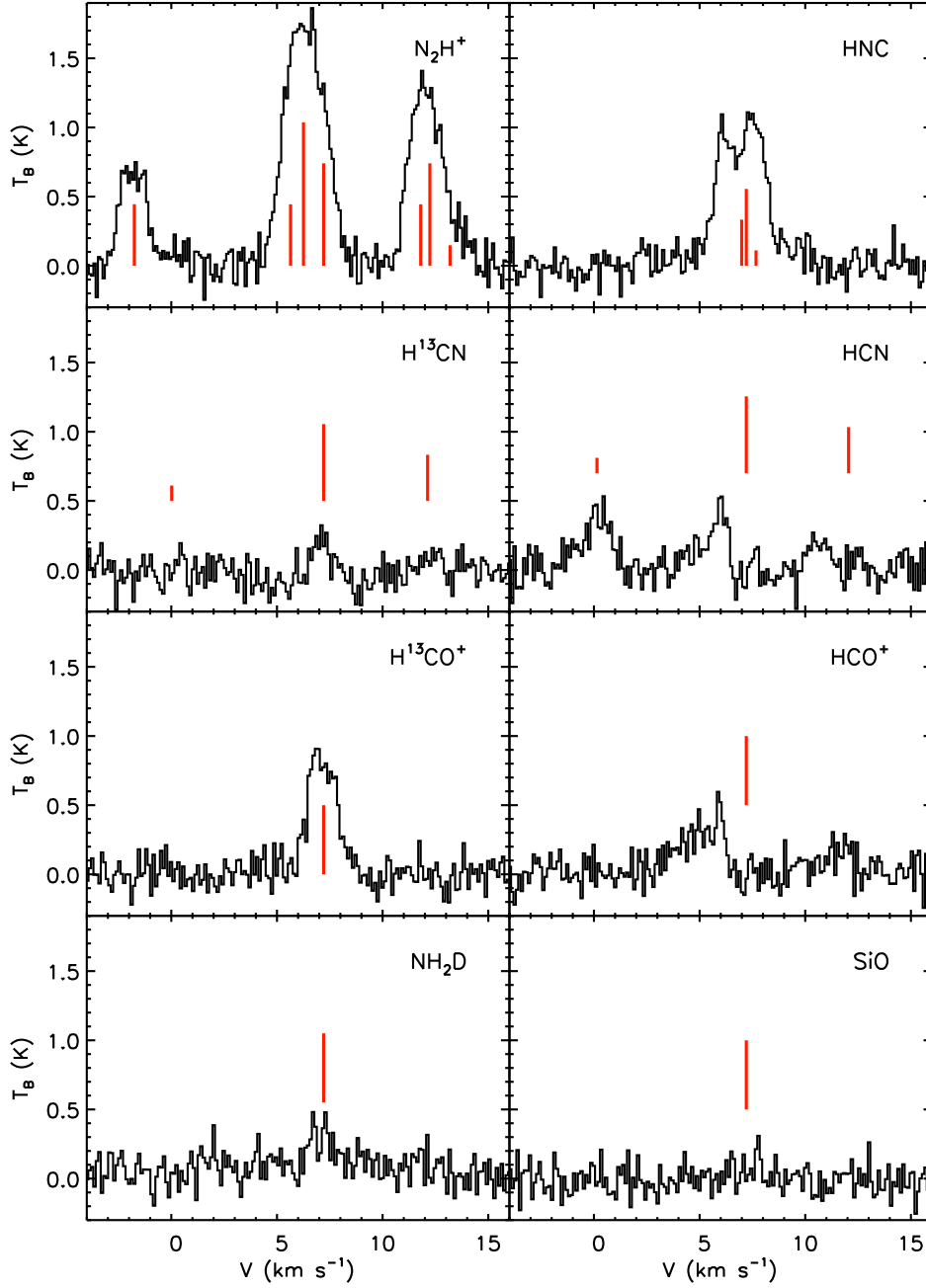
Figure 2. The observed emission lines near the cluster centre ($-18^h30^m01^s, -2^o03'12$"). The data have been summed over 4x4 pixels (an area of 60 by 60$''$) to increase the signal to noise level. The red vertical lines indicate the expected line centres based on a fit to the N$_2$H$^+$ spectrum. In the case of (discernable) hyperfine components, all are shown, with the relative heights scaling with the optically thin line ratios. Note that SiO emission was not detected with certainty anywhere in the map.
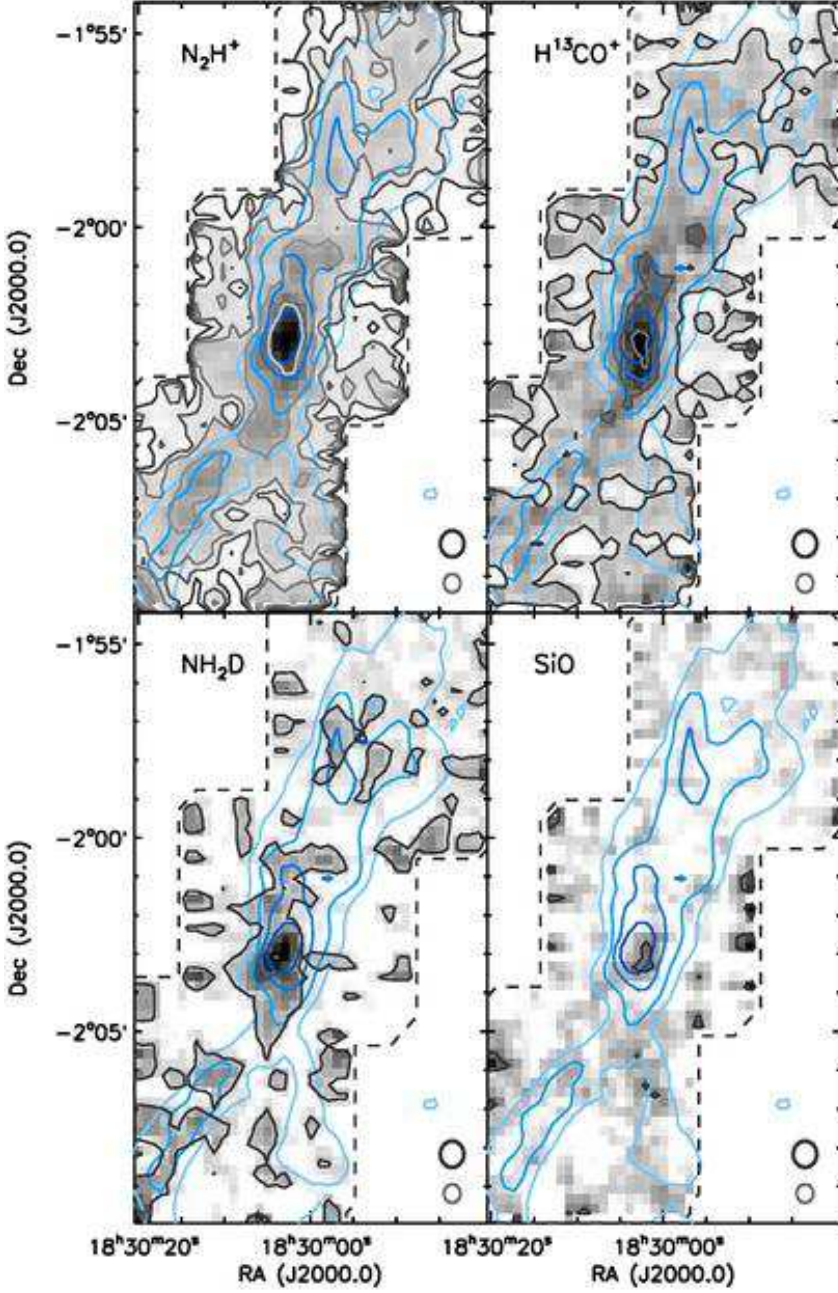
Figure 3. The integrated intensity of the three brightest molecular tracers in our survey not affected by self-absorption (N_2H^+, $H^{13}CO^+$, NH_2D), as well as SiO, which should not show self-absorption, but has no clearly detected emission. The greyscale images show the integrated intensities, with white at a value of -0.1 K km s^{-1} and black at a value of 90% of the maximum integrated intensities measured in each molecular species (23.5, 3.8, 3.2, and 1.2 K km s^{-1} respectively). The grey contours in all panels are at values of 0.5, 2, 3.5, 7, and 15 K km s^{-1} from darkest to lightest. The dashed line indicates the full region mapped by Mopra, and the blue contours show the dust emission from AzTEC/ASTE, at levels of 0.25, 0.5, 1, and 2 Jy bm^{-1} from light to dark. The Mopra and AzTEC/ASTE beams are shown on the bottom right of each panel in dark and light grey respectively.
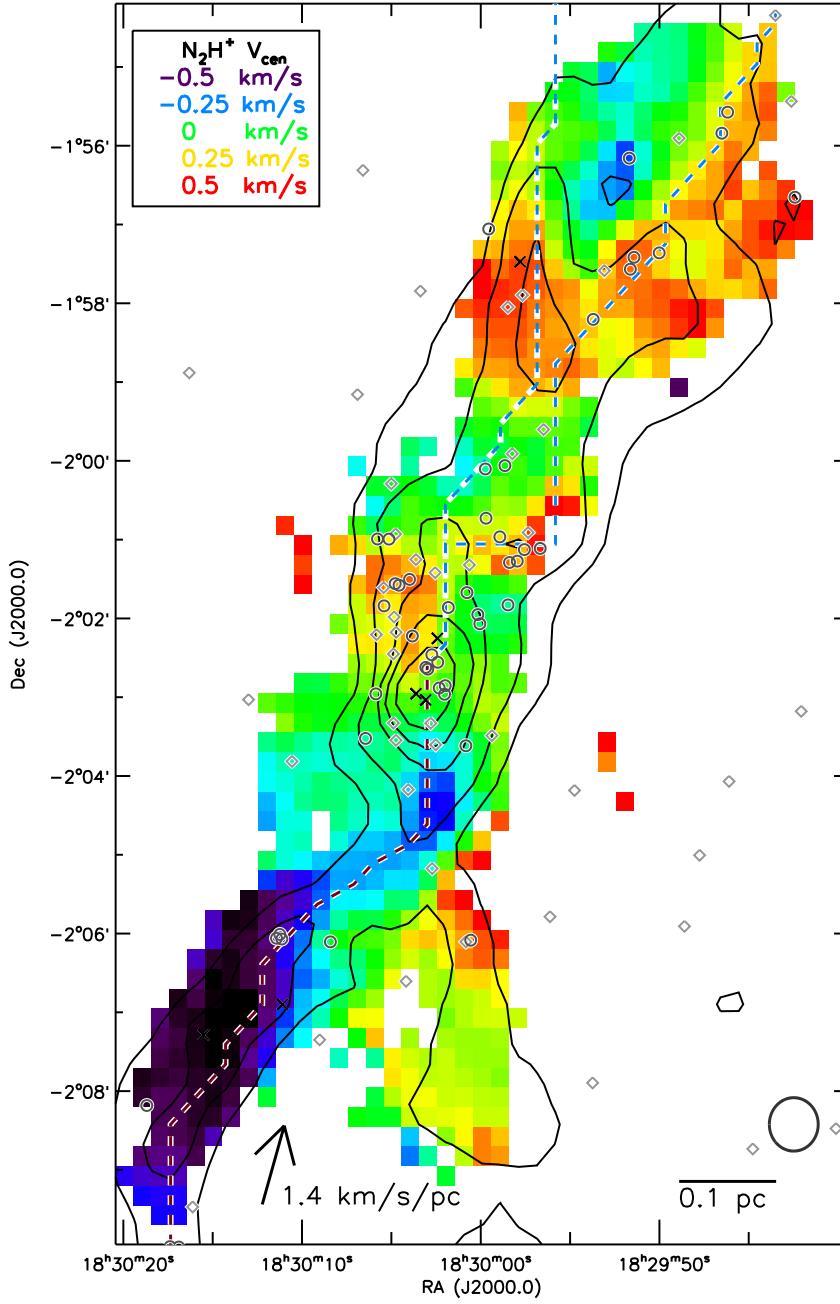
Figure 4. The centroid velocity measured for N_2H^+ across Serpens South. The contours correspond to the dust emission levels shown in Figure 1 and 3, and the circles denote the same YSOs as shown in Figure 1 (dark grey corresponds to class 0, medium grey to class I and light grey to class II sources). The peak ridge of the filament is shown by the dashed lines (red in the south and blue in the north for clarity). The overall velocity gradient measured in the southern filament is indicated by the arrow at the bottom left, while the circle at the bottom right indicates the Mopra beamsize.
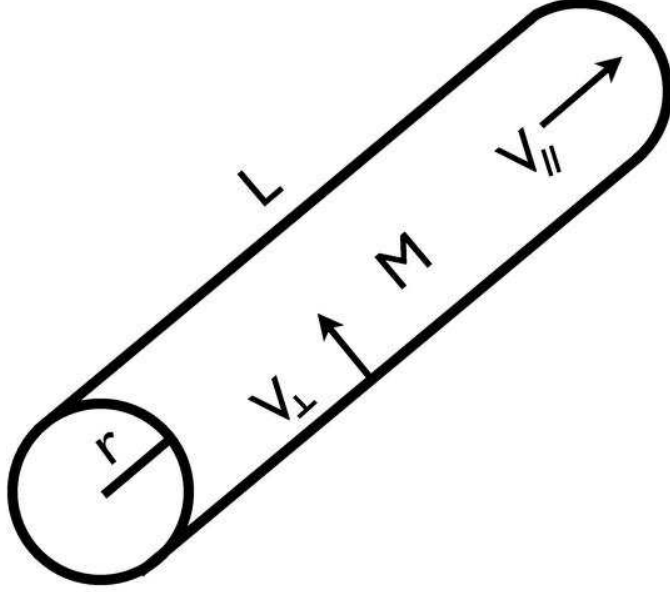
Figure 5. The toy cylinder model we consider for our accretion rate analysis. The cylinder has length L, radius r, mass M, and velocities of $V_\parallel$ along the long axis and $V_\perp$ in the radial direction. It is inclined an angle of α (not shown) relative to the plane of the sky (with the top end further from the observer).
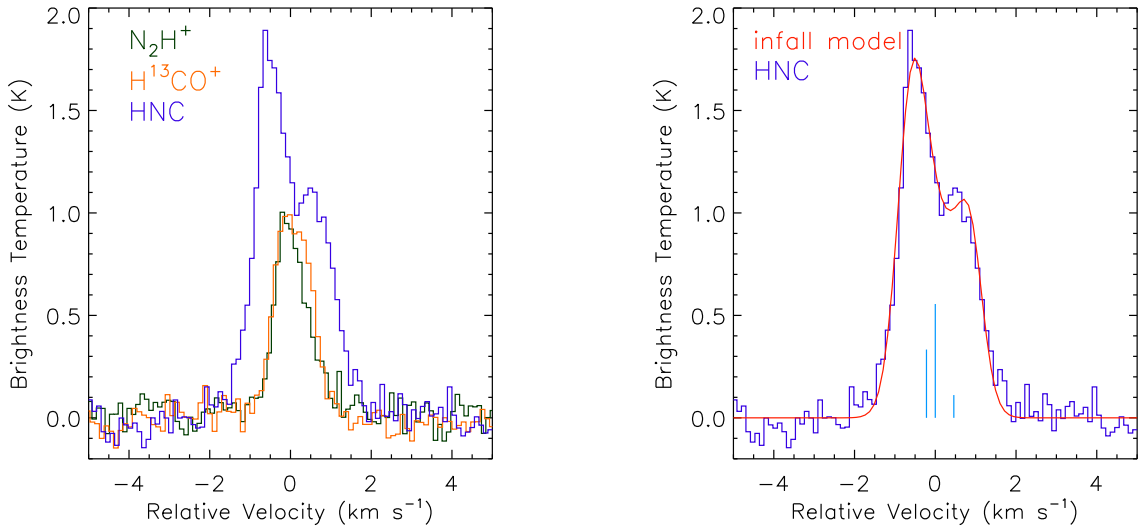

Figure 6. Left: the N_2H^+ (green) and $H^{13}CO^+$ (yellow), and HNC (blue) average spectra for the southern filament. (For N_2H^+, only the isolated hyperfine component, (F_1,F=0,1-1,2), is shown.) The HNC spectrum shows clear signs of self-absorption, while the N_2H^+ and $H^{13}CO^+$ spectra are well described by a single Gaussian. Right: The filament-averaged HNC profile, along with the expected relative positions and strengths of the hyperfine emission lines of HNC. The hyperfine splitting is on too small a scale to be responsible for the observed self-absorption profile. The red line shows the best fit Hill5 infall model profile (deVries & Myers 2005). See text for details.
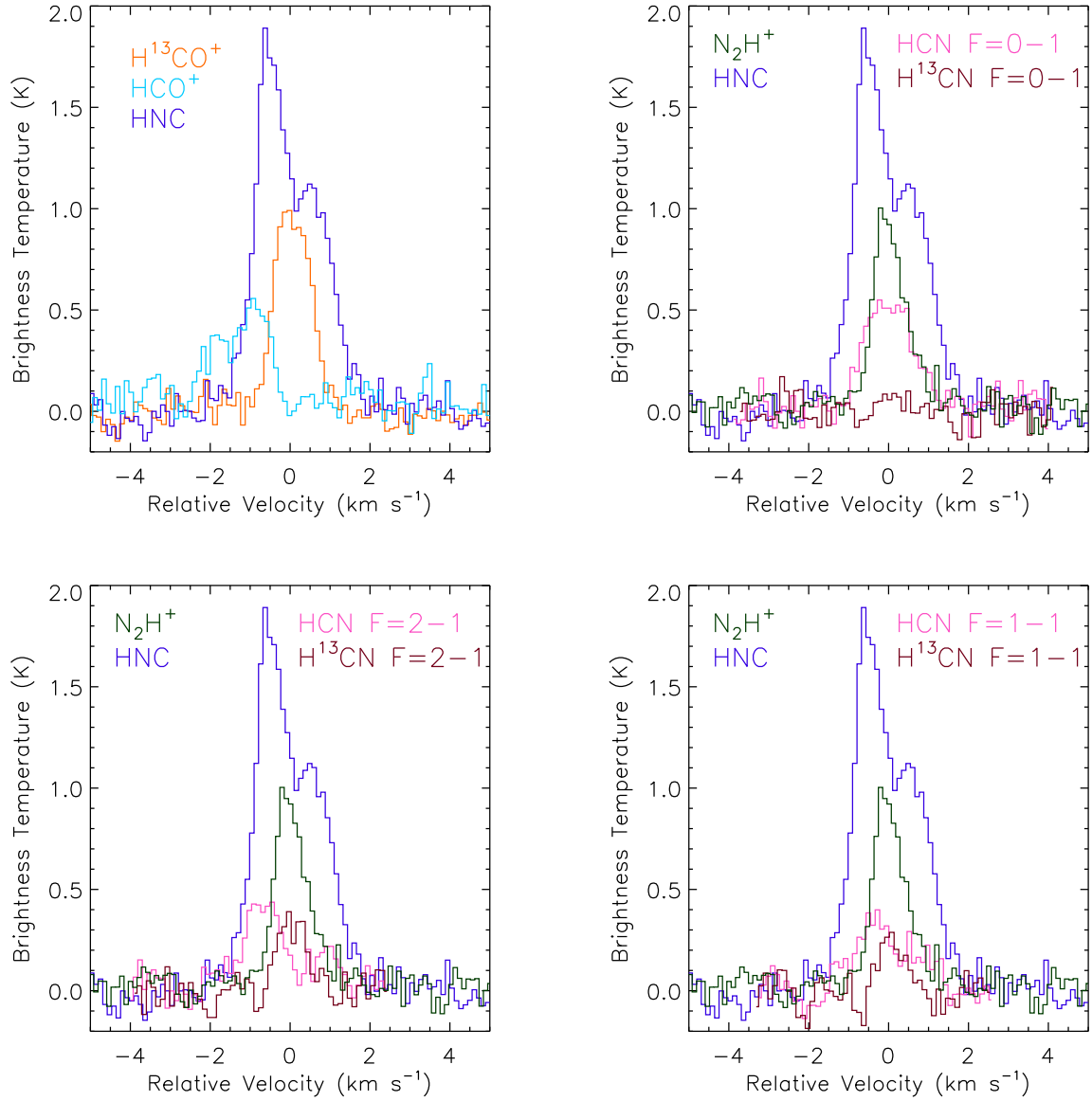
Figure 7. A comparison of the self-absorption profiles for HCO$^+$, and the three hyperfine components of HCN. The HNC emission is shown in dark blue, while H^{13}CO$^+$ is in orange, the isolated hyperfine component of N$_2$H$^+$ (F$_1$,F=0,1-1,2) is in green, HCO$^+$ is shown in light blue, and each component of HCN / H^{13}CN is shown in light / dark pink. In the case of lines with hyperfine components, the velocity centroid has been shifted to the appropriate common centre. Note that no scaling has been applied to the brightness temperatures shown.
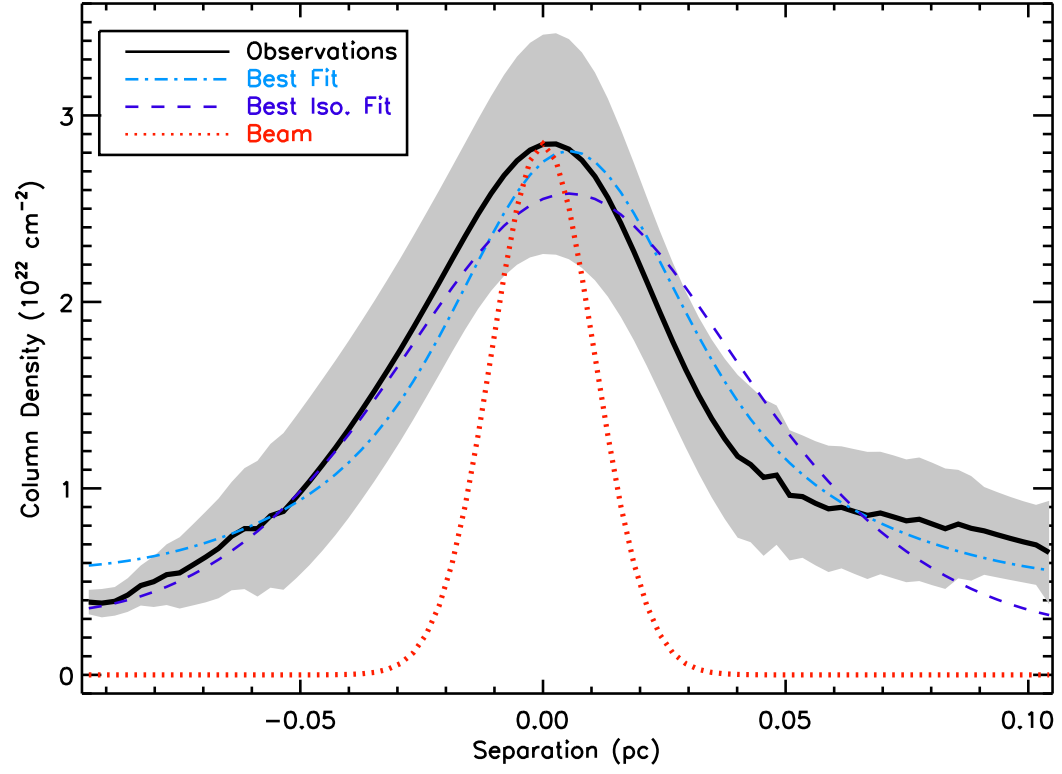
Figure 8. The radial column density profile of the southern filament in Serpens South. The solid black line shows the mean profile across the filament, while the grey shaded area indicates the standard deviation. The AzTEC/ASTE beamsize is shown by the red dotted line. The light blue dash-dotted line shows the best fit profile, following the formulation in Arzoumanian et al (2011), while the dark blue dashed line indicates the best fit profile when the power law index is that corresponding to an isothermal cylinder.